INTERNATIONAL JOURNAL FOR NUMERICAL METHODS IN FLUIDS
Int. J. Numer. Meth. Fluids **26**: 1107–1123 (1998)

NON-HOMOGENEOUS RADIATION AND OUTFLOW BOUNDARY CONDITIONS SIMULATING INCOMING ACOUSTIC AND VORTICITY WAVES FOR EXTERIOR COMPUTATIONAL AEROACOUSTICS PROBLEMS

CHRISTOPHER K.W. TAM*, JUN FANG AND KONSTANTIN A. KURBATSKII

Department of Mathematics, Florida State University, Tallahassee, FL 32306-4510, USA

SUMMARY

A set of non-homogeneous radiation and outflow boundary conditions which automatically generate prescribed incoming acoustic or vorticity waves and, at the same time, are almost transparent to outgoing sound waves produced internally in a finite computation domain is proposed. This type of boundary condition is needed for the numerical solution of many exterior aeroacoustics problems. In computational aeroacoustics, the computation scheme must be as non-dispersive and non-dissipative as possible. It must also support waves with wave speeds which are nearly the same as those of the original linearized Euler equations. To meet these requirements, a high-order/large-stencil scheme is often necessary. The proposed non-homogeneous radiation and outflow boundary conditions are designed primarily for use in conjunction with such high-order/large-stencil finite difference schemes. © 1998 John Wiley & Sons, Ltd.

KEY WORDS: computational aeroacoustics; radiation boundary conditions; scattering of sound or vorticity waves; high-order finite difference solutions

1. INTRODUCTION

Many exterior aeroacoustic problems involve incoming acoustic or vorticity waves interacting with an aircraft engine or the body of the aircraft. An example of this type of problem that is of current interest is the noise generation by the ingestion of free stream turbulence into a fan engine. Another example is the scattering and shielding of sound waves by aircraft wings and fuselage. To simulate these problems using computational aeroacoustics methods, the incoming acoustic and vorticity waves must be generated by the boundary conditions imposed at the outer boundaries of the finite computation domain. In this paper, a set of non-homogeneous radiation and outflow boundary conditions are proposed, which, when used in conjunction with a high-order finite difference scheme, automatically generate the desired incoming acoustic and vorticity waves.

In the presence of a uniform mean flow, the linearized Euler equations support three independent types of small amplitude disturbances. They are the acoustic, the vorticity and the entropy waves. These waves, to linear order, are uncoupled and propagate with different characteristics and wave speeds (see e.g. Reference [1]). In the computational aeroacoustics literature, there seems to be an absence of good suggestions as to how to generate such disturbances in the form of incoming waves.

* Correspondence to: Department of Mathematics, Florida State University, Tallahasse, FL32306-4510, USA.

CCC 0271–2091/98/091107–17$17.50

Received 13 June 1996
Revised 6 June 1997

It is well-known that the solutions of finite difference equations do not perfectly approximate those of the original partial differential equations. However, by choosing the stencil coefficients of a high-order (large-stencil) finite difference scheme appropriately, one can be sure that the part of the solution involving low wave numbers or the long waves are adequately reproduced by the finite difference solution. If a seven-point stencil is used, wave components with wavelengths $> 7-8$ mesh spacings fall into this category. On the other hand, the short wave components of the finite difference scheme inevitably behave quite differently from those of the partial differential equation. This has been discussed at lengths in the work of Trefethen [2] and Tam *et al.* [3]. The short waves are pollutants of a numerical solution. To eliminate the numerical short waves, artificial selective damping is often added to the finite difference scheme. The artificial selective damping terms are designed to eliminate the short (large wave number) waves, but leave the long waves practically undisturbed. The short waves are generated primarily at the boundaries of the computation domain, including internal boundaries such as solid surfaces. The generation of excessive short waves especially the grid-to-grid oscillations at a boundary usually leads to numerical instability. One way to suppress this type of instability is to add stronger artificial damping in the boundary regions. A large symmetric stencil would not fit near a boundary, therefore, shorter damping stencils are used for mesh points adjacent to the boundary. A set of optimized damping stencil coefficients can be found in a recent review article by Tam [4].

For many finite difference schemes, the addition of artificial damping terms often lead to mode coupling. That is, the acoustic, vorticity and entropy wave modes of the numerical scheme are no longer independent. This type of coupling is undesirable. It leads to the gradual degradation of an incoming acoustic wave into an entropy or vorticity wave, as the acoustic wave propagates across the computation domain. When simulating an incoming vorticity wave, it could lead to the generation of spurious acoustic waves, especially at the boundary regions of the computation domain.

There will be discretization error if a finite difference scheme is used to determine the wave solution of partial differential equations. The exact solution of the finite difference equation is not equal to the exact solution of the partial differential equations. In trying to simulate an incoming acoustic or vorticity wave computationally, it is best to reproduce the exact acoustic or vorticity wave solution of the finite difference equations. In this paper, the main issue is not whether the exact finite difference solution is a good approximation of that of the original partial differential equation. It is assumed that it is a good approximation, because a high-order finite difference algorithm used. The aim of this work is how to generate an incoming wave through the imposition of non-homogeneous boundary conditions on a finite computation domain, such that it is almost identical to the exact incoming wave solution of the finite difference equations in an infinite domain.

In this work, the dispersion-relation-preserving (DRP) scheme of Tam and Webb [1] is used for numerical computation. There are two reasons for choosing the DRP scheme. First, the DRP scheme was designed so that the dispersion relations of the finite difference equations are always formally identical to those of the original partial differential equations. Not only does this make the waves supported by the numerical scheme an excellent approximation of those of the partial differential equations, but it also assures that there will be no wave mode coupling in the numerical simulation. The second reason for choosing the DRP scheme is that the exact plane acoustic, vorticity and entropy wave solutions of the finite difference equations can be found analytically. This is discussed in Section 2 of this paper. These exact solutions are used in formulating the non-homogeneous radiation and outflow boundary conditions.

Over the years, there have been a number of investigations devoted to the development of radiation/non-reflecting boundary conditions, but without incoming waves. One group of investigators used asymptotic solutions to construct radiation boundary conditions. These investigators include Bayliss and Turkel [5,6], Hagstrom and Hariharan [7], Hariharan *et al.* [8], Tam and Webb [1], and Tam and Dong [9], to mention a few. Another group used the idea of characteristics. These investigators include Thompson [10,11] and Poinsot and Lele [12]. Still another group devised ways of constructing absorbing boundary conditions to minimize the reflection of waves off the artificial boundary of the computation domain. Investigators of this group are Engquist and Majda [13,14], Higdon [15,16], Jiang and Wong [17], Kosloff and Kosloff [18], and Colonius *et al.* [19]. Givoli [20] wrote a review article on this subject with extensive references.

Recently, Hixon *et al.* [21] performed a detailed evaluation of the suitability of using the Thompson [10,11] quasi-one-dimensional characteristic boundary condition, the Giles [22] Fourier mode decomposition boundary treatment and the asymptotic boundary conditions of Tam and Webb [1] for computational aeroacoustics applications. They concluded that for their test problem, the radiation and outflow boundary conditions of Tam and Webb gave the least reflections and provided the only acceptable boundary treatment. Their recommendations are followed in this work, and the asymptotic boundary conditions of Tam and Webb are used to develop the non-homogeneous radiation, inflow and outflow boundary conditions that would automatically produce very accurate incoming acoustic and vorticity waves in a finite computation domain.

2. ACOUSTIC AND VORTICITY WAVES ON A GRID

Small amplitude disturbances superimposed on a uniform mean flow of Mach number M are considered, as shown in Figure 1. Such disturbances are governed by the linearized Euler equations. Dimensionless variables with length scale $= \Delta x = \Delta y$ (the mesh spacing), velocity scale $= a_0$ (speed of sound), time scale $= \Delta x/a_0$, and pressure scale $= \rho_0 a_0^2$ (where ρ_0 is the gas density) are used. The dimensionless linearized Euler equations are

$$\frac{\partial \mathbf{F}}{\partial t} + \mathbf{R}\frac{\partial \mathbf{F}}{\partial x} + \mathbf{S}\frac{\partial \mathbf{F}}{\partial y} = 0, \tag{2.1}$$

where $\mathbf{F}$, the solution vector, and matrices $\mathbf{R}$ and $\mathbf{S}$ are

$$\mathbf{F} = \begin{bmatrix} u \\ v \\ p \end{bmatrix}, \qquad \mathbf{R} = \begin{bmatrix} M_x & 0 & 1 \\ 0 & M_x & 0 \\ 1 & 0 & M_x \end{bmatrix}, \qquad \mathbf{S} = \begin{bmatrix} M_y & 0 & 0 \\ 0 & M_y & 1 \\ 0 & 1 & M_y \end{bmatrix}. \tag{2.2}$$

In Equation (2.2), M_x and M_y are the mean flow Mach numbers in the x- and y-directions. If ϕ is the direction of the mean flow measured from the x-axis, then $M_x = M\cos\phi$, $M_y = M\sin\phi$.

Upon discretizing Equation (2.1) according to the DRP scheme, the finite difference equations may be written in the following form

$$\mathbf{F}_{\ell,m}^{(n+1)} = \mathbf{F}_{\ell,m}^{(n)} + \Delta t \sum_{j=0}^{3} b_j \mathbf{K}_{\ell,m}^{(n-j)}. \tag{2.3}$$

Subscripts (ℓ, m) are the spatial indices of the mesh in the x- and y-directions. Superscript n is the time level. Δt is the time step. The vector $\mathbf{K}^{(n)}_{\ell,m}$ is given by

$$\mathbf{K}^{(n)}_{\ell,m} = -\mathbf{R}\sum_{j=-3}^{3} a_j \mathbf{F}^{(n)}_{\ell+j,m} - \mathbf{S}\sum_{j=-3}^{3} a_j \mathbf{F}^{(n)}_{\ell,m+j} - \frac{1}{R_{\Delta x}}\sum_{j=-3}^{3} d_j(\mathbf{F}^{(n)}_{\ell+j,m} + \mathbf{F}^{(n)}_{\ell,m+j}). \tag{2.4}$$

The last sum on the right side of (2.4) is the artificial damping terms. $R_{\Delta x}$ is the mesh Reynolds number. The numerical values of the stencil coefficients a_j, b_j and d_j may be found in Reference [4].

The plane wave solutions of finite difference Equations (2.3) and (2.4) are sought over an infinite mesh. The analytical form of the finite difference solution is

$$\mathbf{F}^{(n)}_{\ell,m} = Re\{\hat{\mathbf{F}}\, e^{i(\alpha\ell + \beta m - \omega n\Delta t)}\}. \tag{2.5}$$

In (2.5), $Re\{\ \}$ is the real part. $\hat{\mathbf{F}}$ is the wave amplitude vector (a constant vector). (α, β) are the wave numbers. ω is the angular frequency. Substituting Equation (2.5) into (2.3) and (2.4), after some algebra, the following matrix equation for $\hat{\mathbf{F}}$ is derived.

$$\mathbf{A}\hat{\mathbf{F}} = \mathbf{0}. \tag{2.6}$$

The matrix $\mathbf{A}$ is equal to

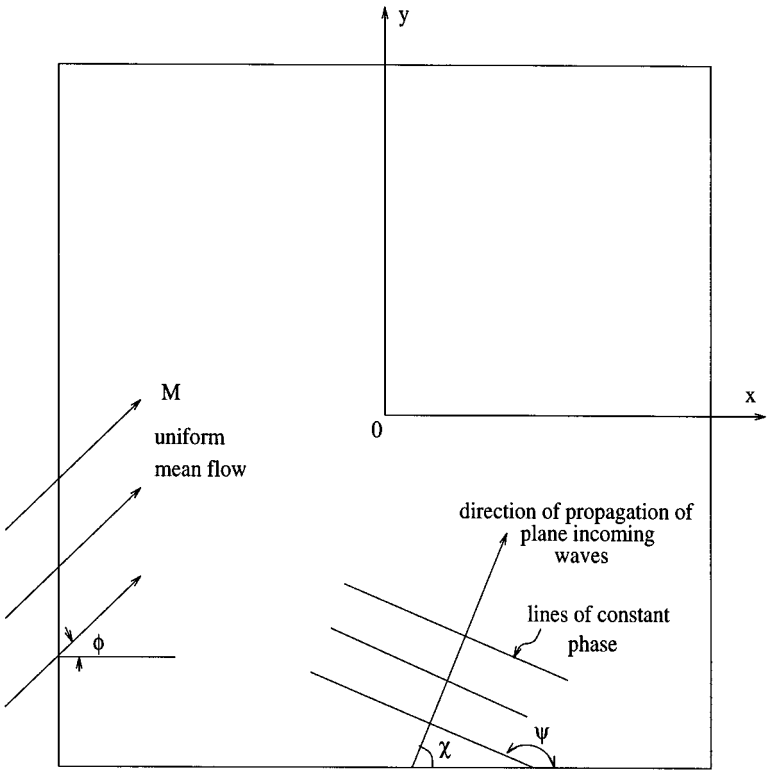

Figure 1. Computational domain showing uniform mean flow and the direction of propagation of incoming plane acoustic or vorticity waves.

$$\mathbf{A} = \begin{bmatrix} -\tilde{\omega} & 0 & \bar{\alpha} \\ 0 & -\tilde{\omega} & \bar{\beta} \\ \bar{\alpha} & \bar{\beta} & -\tilde{\omega} \end{bmatrix}, \tag{2.7}$$

where

$$\tilde{\omega} = \left[\bar{\omega} - M_x\bar{\alpha} - M_y\bar{\beta} + \frac{i(D(\alpha) + D(\beta))}{R_{\Delta x}} \right], \qquad \bar{\alpha} = -i \sum_{j=-3}^{3} a_j \, \mathrm{e}^{ij\alpha},$$

$$\bar{\beta} = -i \sum_{j=-3}^{3} a_j \, \mathrm{e}^{ij\beta}, \qquad \bar{\omega} = \frac{i(\mathrm{e}^{-i\omega\Delta t} - 1)}{\Delta t \sum_{j=0}^{3} b_j \, \mathrm{e}^{ij\omega\Delta t}}, \qquad D(\alpha) = \sum_{j=-3}^{3} d_j \, \mathrm{e}^{-ij\alpha},$$

$$D(\beta) = \sum_{j=-3}^{3} d_j \, \mathrm{e}^{-ij\beta}. \tag{2.8}$$

The quantities $(\bar{\alpha}, \bar{\beta})$ and $\bar{\omega}$ are the wave numbers and angular frequency of the computation scheme [1] (the DRP scheme). $D(\alpha)$ and $D(\beta)$ are the artificial selective damping functions [3,4].

For the non-trivial solution of Equation (2.6), the determinant of the coefficient matrix **A** must be equal to zero. This condition leads to the general dispersion relation

$$\tilde{\omega}(\tilde{\omega}^2 - \bar{\alpha}^2 - \bar{\beta}^2) = 0. \tag{2.9}$$

It should be noted that the dispersion-relation-preserving scheme assures that the dispersion relation (2.9) is the same as that of the waves of the original linearized Euler equations, provided the following substitutions are made: $\bar{\omega} \to \omega$, $\bar{\alpha} \to \alpha$, $\bar{\beta} \to \beta$ and $1/R_{\Delta x} \to 0$.

2.1. Acoustic waves

For acoustic waves, the dispersion relation is obtained by equating the second factor of Equation (2.9) to zero. This gives,

$$\left[\bar{\omega} - M_x\bar{\alpha} - M_y\bar{\beta} + \frac{i(D(\alpha) + D(\beta))}{R_{\Delta x}} \right]^2 - \bar{\alpha}^2 - \bar{\beta}^2 = 0. \tag{2.10}$$

The corresponding eigenvector is

$$\hat{\mathbf{F}} \equiv \begin{bmatrix} F_1 \\ F_2 \\ F_3 \end{bmatrix} = \begin{bmatrix} \bar{\alpha}/\tilde{\omega} \\ \bar{\beta}/\tilde{\omega} \\ 1 \end{bmatrix}. \tag{2.11}$$

Suppose the direction of propagation of the incoming plane acoustic waves is χ (measured from the x-axis), as shown in Figure 1. In this case the direction of propagation is taken to be normal to the lines of constant phase. It follows, therefore, that α and β must be such that

$$\tan\chi = \frac{\beta}{\alpha}. \tag{2.12}$$

A plane acoustic wave may be characterized by its frequency ω and the direction of propagation χ. The wave numbers (α, β) of such a wave can be found by solving Equations (2.10) and (2.12) simultaneously. With the inclusion of artificial damping in the finite difference scheme, Equation (2.4), the wave numbers (α, β) of the wave are complex. Since only a small amount of damping is added, the imaginary parts are small. However, the wave numbers of the corresponding acoustic wave solution of the linearized Euler equations are real. To show

Table I. Wave numbers of acoustic waves $M = 0.5$, $\phi = 30°$, $\chi = 60°$, and $1/R_{\Delta x} = 0.025$

ω	α_{DRP}	β_{DRP}	α_{Euler}	β_{Euler}
0.4	$0.13956+0.133E-04i$	$0.24173+0.231E-04i$	0.13957	0.24174
0.8	$0.27907+0.541E-04i$	$0.48336+0.937E-04i$	0.27913	0.48347
1.0	$0.34875+0.870E-04i$	$0.60405+0.151E-03i$	0.34892	0.60434
1.2	$0.41839+0.132E-03i$	$0.72468+0.229E-03i$	0.41870	0.72521

that the long waves of the DRP scheme (with artificial damping terms) can provide a good approximation to the acoustic wave solution of the linearized Euler equations, let us consider the case $M = 0.5$, $\phi = 30°$, $\chi = 60°$, $1/R_{\Delta x} = 0.025$ and $\Delta t = 0.05$. The wave numbers of the exact solutions of the DRP scheme and the linearized Euler equations are shown in Table I. Table II gives the corresponding eigenvectors (amplitude).

It is easy to see from these tables that the exact acoustic wave solution of the DRP finite difference equations is an excellent approximation of that of the linearized Euler equations. There are at least three figures of accuracy, even for relatively high frequency waves with a wavelength of about eight mesh spacings.

2.2. Vorticity waves

The dispersion relation for the vorticity waves of the finite difference scheme is given by setting $\tilde{\omega}$ to zero in Equation (2.9); i.e.

$$\bar{\omega} - M_x\bar{\alpha} - M_y\bar{\beta} + \frac{i}{R_{\Delta x}}(D(\alpha) + D(\beta)) = 0. \tag{2.13}$$

The corresponding eigenfunction is

$$\hat{\mathbf{G}} \equiv \begin{bmatrix} G_1 \\ G_2 \\ 0 \end{bmatrix} = \begin{bmatrix} \dfrac{\bar{\beta}}{(\bar{\alpha}^2 + \bar{\beta}^2)^{1/2}} \\ \dfrac{-\bar{\alpha}}{(\bar{\alpha}^2 + \bar{\beta}^2)^{1/2}} \\ 0 \end{bmatrix}. \tag{2.14}$$

Let ψ be the angle between the lines of constant phase of the vorticity waves and the x-axis (see Figure 1) then

$$\tan\psi = -\cot\chi = -\frac{\alpha}{\beta}. \tag{2.15}$$

A vorticity wave may be specified by its frequency ω and the phase angle ψ. The wave numbers of such waves are found by solving Equations (2.13) and (2.15) simultaneously.

Table II. Eigenvectors of acoustic waves

ω	u_{DRP}	v_{DRP}	u_{Euler}	v_{Euler}
0.4	$0.49999-0.323E-08i$	$0.86603+0.186E-08i$	0.50000	0.86603
0.8	$0.49989-0.676E-07i$	$0.86609+0.390E-07i$	0.50000	0.86603
1.0	$0.49979-0.132E-06i$	$0.86615+0.760E-07i$	0.50000	0.86603
1.2	$0.49970-0.106E-06i$	$0.86620+0.613E-07i$	0.50000	0.86603

Table III. Wave numbers of vorticity waves $M = 0.5$, $\phi = 30°$, $\psi = 120°$, and $1/R_{\Delta x} = 0.05$

ω	α_{DRP}	β_{DRP}	α_{Euler}	β_{Euler}
0.3	$0.51944+0.269E-03i$	$0.29990+0.155E-03i$	0.51962	0.30000
0.4	$0.69231+0.289E-03i$	$0.39971+0.167E-03i$	0.69282	0.40000
0.5	$0.86527+0.262E-03i$	$0.49956+0.152E-03i$	0.86603	0.50000
0.6	$1.03950+0.391E-03i$	$0.60015+0.225E-03i$	1.03923	0.60000

Because of the inclusion of artificial damping terms, the wave numbers are again complex. Table III provides a numerical example of the case of plane vorticity waves, with $\psi = 120°$ superimposed on a mean flow at $M = 0.5$, $\phi = 30°$, $1/R_{\Delta x} = 0.05$ and $\Delta t = 0.0567$. The corresponding eigenvectors (2.14) are given in Table IV. The numerical values in these tables indicate again that there is excellent agreement between the finite difference (DRP scheme) solution in an infinite mesh and the exact vorticity wave solution of the linearized Euler equations.

3. NON-HOMOGENEOUS RADIATION AND OUTFLOW BOUNDARY CONDITIONS

The procedure for numerical simulation of exterior aeroacoustics problems involving incoming acoustic or vorticity waves is now discussed. By necessity, the computation domain is finite. Without loss of generality, the flow configuration is set as in Figure 1. With the inflow as prescribed, the bottom and the left side of the computation domain constitute the inflow boundaries. The right and top sides are the outflow boundaries.

In the absence of incoming waves, the radiation boundary conditions of Tam and Webb [1], which are the same as those of Bayliss and Turkel [5], may be imposed along the inflow boundaries. In polar co-ordinates (r, θ) with the origin at the center of the computation domain, these radiation boundary conditions for the outgoing waves, $\mathbf{F}_{\mathrm{out}}$, may be written as,

$$\frac{\partial \mathbf{F}_{\mathrm{out}}}{\partial t} = -V(\theta)\left(\frac{\partial}{\partial r} + \frac{1}{2r}\right)\mathbf{F}_{\mathrm{out}}. \tag{3.1}$$

The acoustic wave propagation velocity $V(\theta)$ of Equation (3.1) is equal to,

$$V(\theta) = M\cos(\theta - \phi) + [1 - M^2\sin(\theta - \phi)]^{1/2}. \tag{3.2}$$

Along the outflow boundaries, Tam and Webb showed that the outgoing disturbances may be comprised of acoustic, vorticity and entropy waves. By means of the asymptotic solutions of these waves, they demonstrated that for pressure, p_{out}, the outflow boundary condition is the

Table IV. Eigenvectors of vorticity waves

ω	u_{DRP}	v_{DRP}	u_{Euler}	v_{Euler}
0.3	$0.49986-0.259E-03i$	$-0.86610-0.449E-08i$	0.50000	-0.86603
0.4	$0.49972-0.209E-03i$	$-0.86619-0.363E-07i$	0.50000	-0.86603
0.5	$0.49975-0.152E-03i$	$-0.86617-0.262E-07i$	0.50000	-0.86603
0.6	$0.50045-0.188E-03i$	$-0.86576-0.319E-07i$	0.50000	-0.86603

same as in Equation (3.1). For the velocity components, $(u_{\text{out}}, v_{\text{out}})$, the approximate outflow boundary conditions are,

$$\frac{\partial}{\partial t}\begin{bmatrix} u_{\text{out}} \\ v_{\text{out}} \end{bmatrix} = -\left[M_x \frac{\partial}{\partial x} + M_y \frac{\partial}{\partial y} \right] \begin{bmatrix} u_{\text{out}} \\ v_{\text{out}} \end{bmatrix} - \begin{bmatrix} \dfrac{\partial}{\partial x} \\ \dfrac{\partial}{\partial y} \end{bmatrix} p_{\text{out}}. \tag{3.3}$$

3.1. Incoming acoustic waves

As discussed in Section 2, an incoming plane acoustic wave on a grid has a mathematical solution in the form

$$\begin{bmatrix} u \\ v \\ p \end{bmatrix}^{(\mathrm{n})}_{\ell,m} \equiv \mathbf{F} = Re\{\hat{\mathbf{F}}\, \mathrm{e}^{i(\alpha \ell + \beta m - \omega n \Delta t)}\}, \tag{3.4}$$

where $\hat{\mathbf{F}}$, the eigenvector, is given by Equation (2.11) and the wave numbers (α, β) are found by solving (2.10) and (2.12) simultaneously. Let $\mathbf{F}^{(n)}_{\ell,m}$ be the numerical solution of the discretized linearized Euler equations. At the inflow boundaries, $\mathbf{F}^{(n)}_{\ell,m}$ is made up of the incoming and the outgoing acoustic waves. By subtracting $\mathbf{F}$ of Equation (3.4) from $\mathbf{F}^{(n)}_{\ell,m}$, the outgoing acoustic wave solution, $\mathbf{F}_{\text{out}}$, is

$$\mathbf{F}_{\text{out}} = \mathbf{F}^{(n)}_{\ell,m} - \mathbf{F}. \tag{3.5}$$

Now $\mathbf{F}_{\text{out}}$, being purely outgoing waves, must satisfy radiation boundary condition (3.1). It is to be noted that $\mathbf{F}$ and $\mathbf{F}^{(n)}_{\ell,m}$ and hence $\mathbf{F}_{\text{out}}$ are defined only on the solution mesh. To implement Equation (3.1), the spatial and time derivatives must be discretized first. Equation (3.1) may be rewritten in the form

$$\frac{\partial}{\partial t}\left[\mathbf{F}^{(n)}_{\ell,m} - Re(\hat{\mathbf{F}}\, \mathrm{e}^{i(\alpha \ell + \beta m - \omega n \Delta t)})\right] = \mathbf{W}, \tag{3.6}$$

where $\mathbf{W}$ is

$$\mathbf{W} = -V(\theta)\left[\cos\theta \frac{\partial}{\partial x} + \sin\theta \frac{\partial}{\partial y} + \frac{1}{2r}\right]\left[\mathbf{F}^{(n)}_{\ell,m} - Re(\hat{\mathbf{F}}\, \mathrm{e}^{i(\alpha \ell + \beta m - \omega n \Delta t)})\right] + \text{damping terms}. \tag{3.7}$$

The discretized form of (3.6) following the DRP scheme is,

$$\mathbf{F}^{(n+1)}_{\ell,m} = \mathbf{F}^{(n)}_{\ell,m} + \Delta t \sum_{j=0}^{3} b_j \mathbf{W}^{(n-j)}_{\ell,m} + Re\{\hat{\mathbf{F}}\, \mathrm{e}^{i(\alpha \ell + \beta m - \omega n \Delta t)}(\mathrm{e}^{-i\omega \Delta t} - 1)\}. \tag{3.8}$$

In the inflow boundary region (see Figure 2); i.e. the bottom three rows and the left-most three columns of mesh points, backward difference stencils are used to approximate the spatial derivatives of (3.7). The particular backward difference stencils to be used depend on the location of the point relative to the boundary of the computation domain. For example, for the corner point 'A' with $\ell = L$ and $m = M$ as shown in Figure 2, the discretized form of (3.7) is,

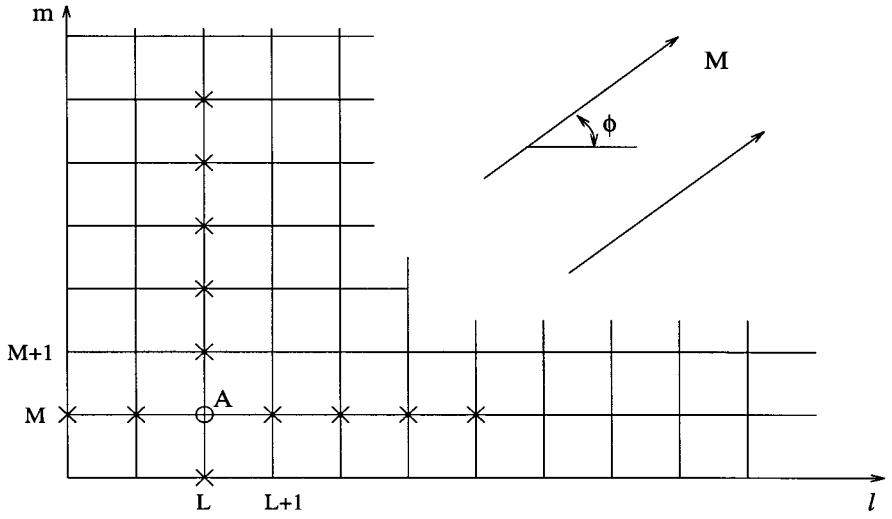

Figure 2. Backward difference stencils used to approximate spatial derivatives in the inflow boundary region of the computational domain.

$$
\begin{aligned}
\mathbf{W}_{L,M}^{(n)} = V(\theta_{L,M})\Bigg\{ & \cos(\theta_{L,M}) \sum_{j=-2}^{4} a_j^{24}[\mathbf{F}_{L+j,M}^{(n)} - Re(\hat{\mathbf{F}}\, \mathrm{e}^{i(\alpha(L+j)+\beta M-\omega n\Delta t)})] \\
& + \sin(\theta_{L,M}) \sum_{j=-1}^{5} a_j^{15}[\mathbf{F}_{L,M+j}^{(n)} - Re(\hat{\mathbf{F}}\, \mathrm{e}^{i(\alpha L+\beta(M+j)-\omega n\Delta t)})] \\
& + \frac{1}{2r_{L,M}}[\mathbf{F}_{L,M}^{(n)} - Re(\hat{\mathbf{F}}\, \mathrm{e}^{i(\alpha L+\beta M-\omega n\Delta t)})]\Bigg\} \\
& - \frac{1}{R_{\Delta x}}\Bigg\{ \sum_{j=-2}^{2} d_j^{(5)}[\mathbf{F}_{L+j,M}^{(n)} - Re(\hat{\mathbf{F}}\, \mathrm{e}^{i(\alpha(L+j)+\beta M-\omega n\Delta t)})] \\
& + \sum_{j=-1}^{1} d_j^{(3)}[\mathbf{F}_{L,M+j}^{(n)} - Re(\hat{\mathbf{F}}\, \mathrm{e}^{i(\alpha L+\beta(M+j)-\omega n\Delta t)})]\Bigg\},
\end{aligned}
\tag{3.9}
$$

where $(r_{L,M}, \theta_{L,M})$ are the polar co-ordinates of the point 'A'. $d_j^{(5)}$ and $d_j^{(3)}$ are the coefficients of the five-point and three-point damping stencils [4]. Equation (3.8), supplemented by formulae for $\mathbf{W}_{\ell,m}^{(n)}$ in the form of (3.9), is the desired non-homogeneous radiation boundary conditions.

On the outflow boundaries, the computed solution (u, v, p) consists of the incoming acoustic waves $\mathbf{F}$ of Equation (3.4), and the as yet unknown outgoing disturbances $(u_{\text{out}}, v_{\text{out}}, p_{\text{out}})$; i.e.

$$
\begin{bmatrix} u_{\text{out}} \\ v_{\text{out}} \\ p_{\text{out}} \end{bmatrix} = \begin{bmatrix} u \\ v \\ p \end{bmatrix} - Re(\hat{\mathbf{F}}\, \mathrm{e}^{i(\alpha\ell+\beta m-\omega n\Delta t)}). \tag{3.10}
$$

The boundary conditions (3.3) should be satisfied by $(u_{\text{out}}, v_{\text{out}}, p_{\text{out}})$, which are purely outgoing disturbances along the outflow boundaries. For p_{out}, the same condition as at the inflow boundaries may be used.

To implement Equation (3.3) with the inclusion of artificial damping terms according to the DRP scheme, first (3.10) is used to recast the equation into the form,

$$\frac{\partial}{\partial t}\left[\begin{matrix}u\\v\end{matrix} - Re\left\{\begin{pmatrix}F_1\\F_2\end{pmatrix} e^{i(\alpha\ell + \beta m - \omega n\Delta t)}\right\}\right] = \mathbf{H}. \tag{3.11}$$

The discretized form of Equation (3.11) is

$$\begin{bmatrix}u\\v\end{bmatrix}_{\ell,m}^{(n+1)} \begin{bmatrix}u\\v\end{bmatrix}_{\ell,m}^{(n)} + \Delta t \sum_{j=0}^{3} b_j \left[\mathbf{H}_{\ell,m}^{(n-j)} + Re\left\{\begin{pmatrix}F_1\\F_2\end{pmatrix} e^{i(\alpha\ell + \beta m - \omega n\Delta t)}(e^{-i\omega\Delta t} - 1)\right\}\right]. \tag{3.12}$$

In developing the discretized form of **H**, backward difference stencils are again used to approximate the spatial derivatives. These stencils may vary from point to point, depending on their location relative to the boundary of the computation domain. For instance, for the boundary point '*B*' in Figure 3, with $\ell = L$ and $m = M$, the discretized function **H**, including the artificial damping terms, is

$$\begin{aligned}\mathbf{H}_{L,M}^{(n)} = &- M_x \sum_{j=-5}^{1} a_j^{51}\left[\begin{matrix}u_{L+j,M}^{(n)}\\v_{L+j,M}^{(n)}\end{matrix} - Re\left\{\begin{pmatrix}F_1\\F_2\end{pmatrix} e^{i[\alpha(L+j)+\beta M - \omega n\Delta t]}\right\}\right]\\ &- M_y \sum_{j=-4}^{2} a_j^{42}\left[\begin{matrix}u_{L,M+j}^{(n)}\\v_{L,M+j}^{(n)}\end{matrix} - Re\left\{\begin{pmatrix}F_1\\F_2\end{pmatrix} e^{i[\alpha L+\beta(M+j) - \omega n\Delta t]}\right\}\right]\\ &- \begin{bmatrix}\sum_{j=-5}^{1} a_j^{51}\{p_{L+j,M}^{(n)} - Re\{F_1\, e^{i[\alpha(L+j)+\beta M - \omega n\Delta t]}\}\}\\ \sum_{j=-4}^{2} a_j^{42}\{p_{L,M+j}^{(n)} - Re\{F_2\, e^{i[\alpha L+\beta(M+j) - \omega n\Delta t]}\}\}\end{bmatrix}\end{aligned}$$

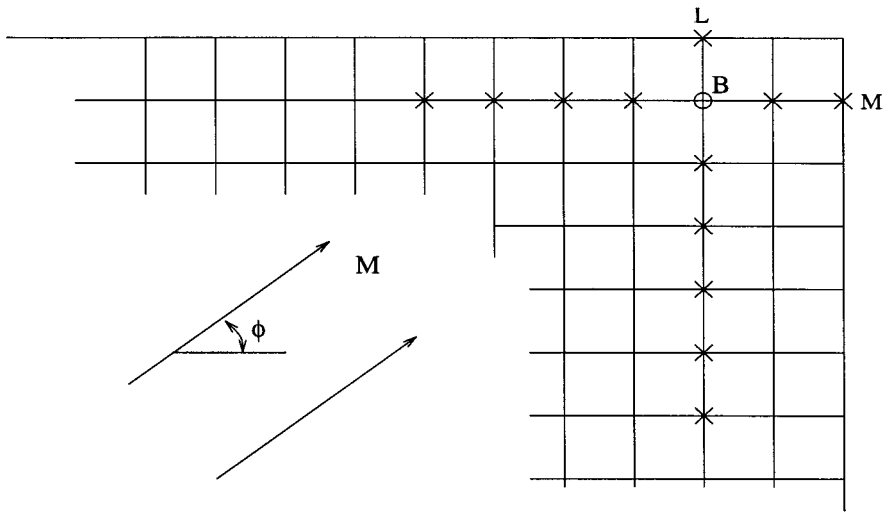

Figure 3. Backward difference stencils used to approximate spatial derivatives in the outflow region of the computational domain.

$$-\frac{1}{R_{\Delta x}}\left\{\sum_{j=-1}^{1} d_j^{(3)}\left[\begin{matrix}u_{L+j,M}^{(n)}\\ v_{L+j,M}^{(n)}\end{matrix}-Re\left\{\begin{pmatrix}F_1\\F_2\end{pmatrix}\mathrm{e}^{i[\alpha(L+j)+\beta M-\omega n\Delta t]}\right\}\right]\right.$$
$$\left.+\sum_{j=-4}^{2} d_j^{(5)}\left[\begin{matrix}u_{L,M+j}^{(n)}\\ v_{L,M+j}^{(n)}\end{matrix}-Re\left\{\begin{pmatrix}F_1\\F_2\end{pmatrix}\mathrm{e}^{i[\alpha L+\beta(M+j)-\omega n\Delta t]}\right\}\right]\right\}. \tag{3.13}$$

Equation (3.12), supplemented by formulas of the form of (3.13), provides the non-homogeneous outflow boundary conditions.

To test whether non-homogeneous radiation boundary conditions (3.8) and (3.9) and outflow boundary conditions (3.12) and (3.13) can generate an accurate plane acoustic wave propagating across the finite computation domain without the simultaneous generation of spurious vorticity or entropy waves, a series of numerical simulations have been carried out. In the simulations, a 100×100 mesh was used. In the interior region, time marching scheme Equations (2.3) and (2.4) were used to time step the solution to a periodic state. Along the inflow boundaries, the variables of the solution were updated using non-homogeneous radiation boundary conditions (3.8) and (3.9). Along the outflow boundaries, non-homogeneous outflow boundary conditions (3.12) and (3.13) were used. Figure 4 shows the time history of convergence to the exact finite difference acoustic wave solution for the case $M = 0.5$, $\phi = 30°$, $\chi = 60°$, $\omega = 1.2$ and $1/R_{\Delta x} = 0.025$. The ordinate is the maximum error, defined as the absolute value of the maximum difference (over the entire computation domain) between the numerical solution and the exact solution of the finite difference equations. The abscissa is the number of time steps. For this simulation, a zero acoustic wave initial condition was used. Over time, the computed solution converges to the exact incoming wave solution to machine accuracy.

Figure 5 shows typical error (in comparison with the exact finite difference solution) of the pressure variable, p, at each mesh point of the finite computation domain at the beginning of an oscillation cycle, after the numerical solution has reached a time periodic state. The error is less than 10^{-13} everywhere. The error of the velocity variables are of a similar order of magnitude.

3.2. Incoming vorticity waves

A set of non-homogeneous radiation and outflow boundary conditions for incoming vorticity waves can be formulated in exactly the same way as discussed above. According to Section 2.2, an incoming vorticity wave on a grid has the mathematical representation of

$$\begin{bmatrix}u\\v\\p\end{bmatrix} \equiv \mathbf{G} = Re\{\hat{\mathbf{G}}\,\mathrm{e}^{i(\alpha\ell+\beta m-\omega n\Delta t)}\}, \tag{3.14}$$

where $\hat{\mathbf{G}}$ is given by Equation (2.14), and (α, β) are the simultaneous solution of (2.14) and (2.15). It should be noted that the main difference between an incoming vorticity wave and an acoustic wave is the replacement of $\mathbf{F}$ of Equation (3.4) by $\mathbf{G}$ of (3.14). It is clear, therefore, that the desired non-homogeneous radiation boundary conditions for an incoming vorticity wave can be found by the substitution of $\mathbf{F}$ by $\mathbf{G}$ in the non-homogeneous terms of (3.8) and (3.9). Similarly, by replacing $\mathbf{F}$ by $\mathbf{G}$ in Equations (3.12) and (3.13), the corresponding non-homogeneous outflow boundary conditions are obtained.

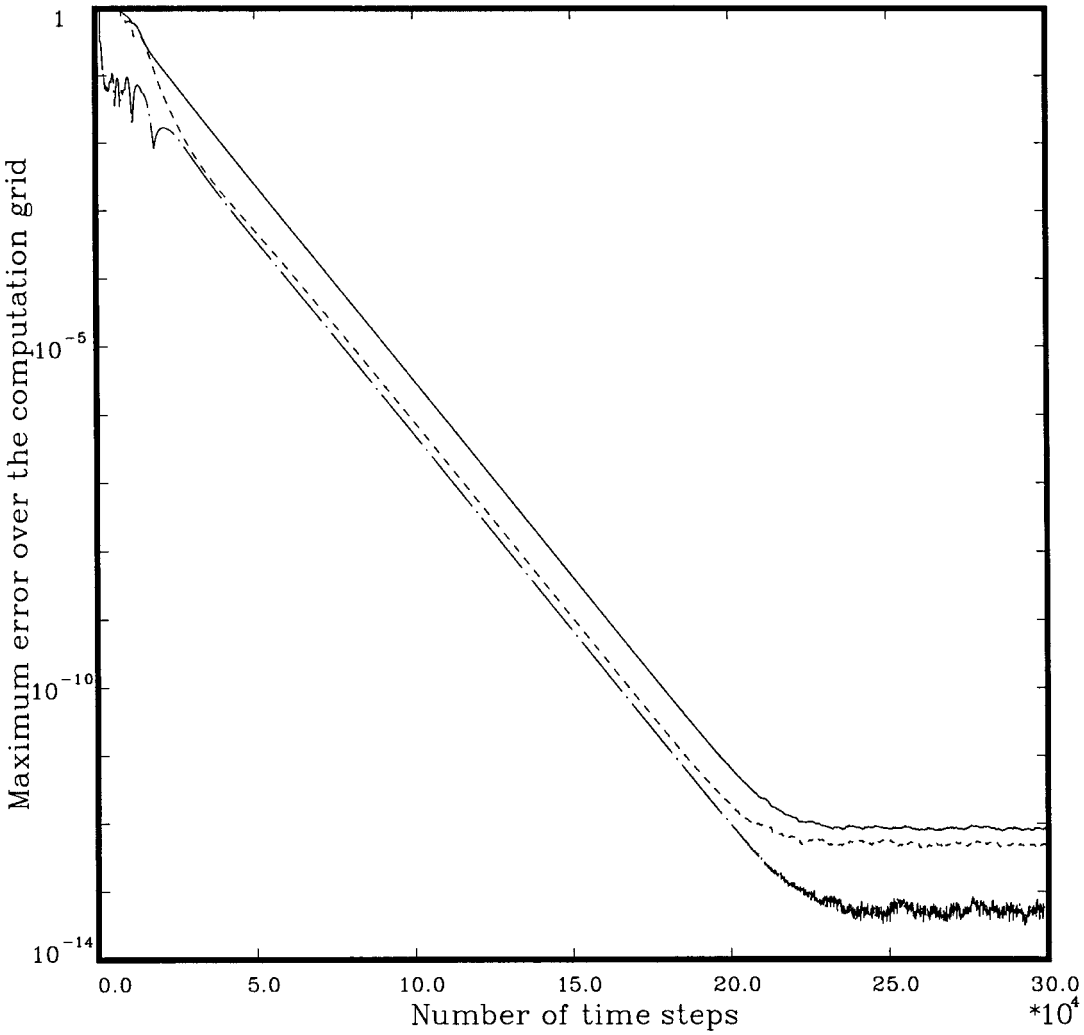

Figure 4. Convergence history of direct numerical simulation of incoming acoustic wave on a 100×100 grid. $M = 0.5$, $\phi = 30°$, $\chi = 60°$, $\omega = 1.2$, $1/R_{\Delta x} = 0.025$. —— u, - - - - v, – · – · – · – p.

A series of numerical simulations for an incoming vorticity wave superimposed on a uniform mean flow has been carried out using a 100×100 grid. The convergence history for the case $M = 0.5$, $\phi = 30°$, $\psi = 120°$, $\omega = 0.4$ and $1/R_{\Delta x} = 0.025$ is similar to that of Figure 4. The error is again very small everywhere, with a distribution similar to that of Figure 5.

4. APPLICATIONS

This section reports the results of applying the non-homogeneous radiation and outflow boundary conditions developed in the previous section to the numerical simulation of the scattering of plane acoustic waves by a cylinder and the generation of sound by the interaction of a flat plate in a gust.

4.1. Scattering of acoustic waves by a solid cylinder

The problem of the scattering of acoustic waves by a solid cylinder was simulated numerically in the time domain. The incoming acoustic waves were generated by the non-homogeneous radiation boundary conditions of Section 3. A 320×320 mesh was used in the computation. The cylinder with a diameter of 32 was placed in the center of the computation domain as shown in Figure 6. Plane acoustic waves with a wave length of eight mesh spacings entered the computation domain from the left boundary. In the numerical simulation, the linearized Euler equations were solved using the DRP scheme (Equations (2.3) and (2.4)). A Cartesian boundary treatment using ghost values of pressure to enforce the solid surface boundary condition of zero normal fluid velocity, developed recently by Kurbatskii and Tam [23], was applied around the surface of the cylinder. A zero acoustic wave initial condition was used to start the computation. The solution was marched in time until a time periodic state was reached.

Figure 6 shows the contours of zero pressure obtained by the numerical simulation. The zero pressure contours of the exact solution are also plotted in this figure as dotted curves. There is good agreement between the numerical and the exact solution, so that the two sets of curves are almost indistinguishable. In Figure 6, the shadow zone behind the cylinder shows up

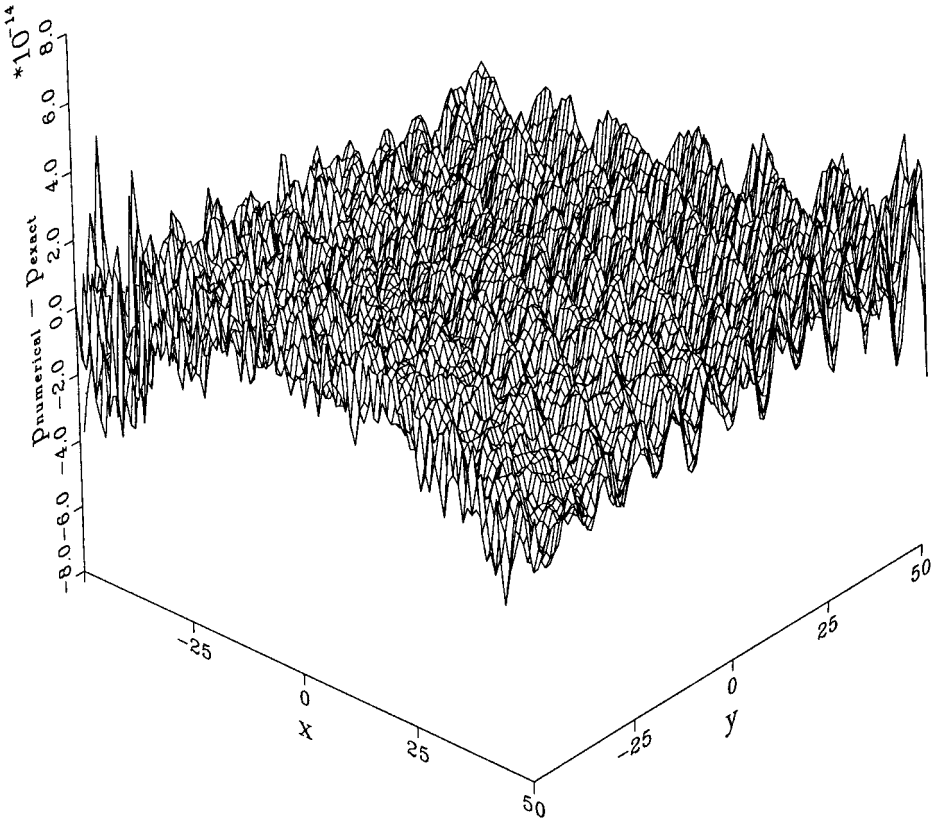

Figure 5. Perspective diagram showing error in p at each grid point at the beginning of a cycle of oscillation after the incoming acoustic wave solution has been established over the entire computation domain. $M = 0.5$, $\phi = 30°$, $\chi = 60°$, $\omega = 1.2$.

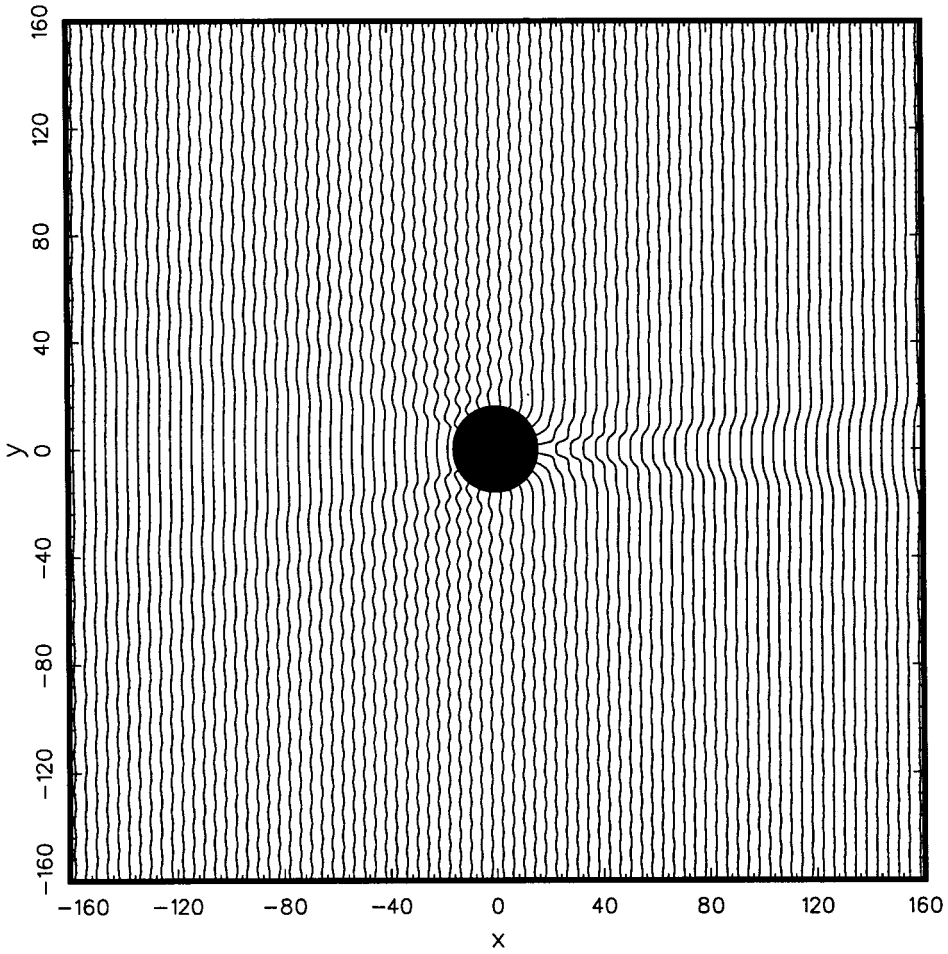

Figure 6. Map of the zero pressure contours at the beginning of a cycle associated with the scattering of plane acoustic waves by a solid cylinder. Wavelength $= 8\Delta x$, diameter of the cylinder $= 32\Delta x$.

prominently. There are strong scattered waves propagating backwards to the two sides of the cylinder. They are responsible for the wiggles of the zero pressure contours of the figure. The good agreement between the numerical and exact solution provides strong evidence that the proposed non-homogeneous radiation boundary conditions are accurate and effective.

4.2. Sound generation by the interaction of a flat plate in a gust

As another application of the non-homogeneous radiation and outflow boundary conditions, numerical simulations of sound generation by the interaction of a flat plate in a gust (vorticity waves) were performed. The case of $M = 0.5$ and a vertical gust with

$$u = 0, \qquad v = 0.1 \sin\left[\frac{\pi}{8}\left(\frac{x}{M} - t\right)\right],$$

as shown in Figure 7 was considered. A 200×200 mesh was used. The flat plate had a length of 30. It was located on the x-axis in the center of the computation domain. The incoming

vorticity waves were convected into the computation domain by the mean flow from the left boundary. The DRP time marching scheme was again used. The wall boundary condition on the plate was enforced by the ghost point method. Non-homogeneous radiation boundary conditions were imposed on the left, top and bottom boundary regions. Non-homogeneous outflow boundary conditions were imposed on the right boundary. The numerical solution was time stepped from a zero vorticity wave initial condition until a time periodic state was established.

Figure 8 shows the computed directivity of acoustic radiation in the top half-plane. No exact solution of the present problem is available for comparison. Also shown in this figure are the computed directivities using two and three times the original spatial resolution. It is clear from the numerical results that there is numerical convergence. This gust-plate interaction problem is a generic turbomachinery noise problem. Direct numerical simulation of this problem as a scattering problem in the time domain has never been carried out before.

5. CONCLUSIONS

A set of non-homogeneous radiation and outflow boundary conditions designed for use in conjunction with high-order/large-stencil finite difference schemes has been developed. The non-homogeneous boundary conditions generate the desired incoming acoustic or vorticity waves and, at the same time, allow the scattered or internally generated disturbances to leave the computation domain with almost no reflections. These non-homogeneous boundary

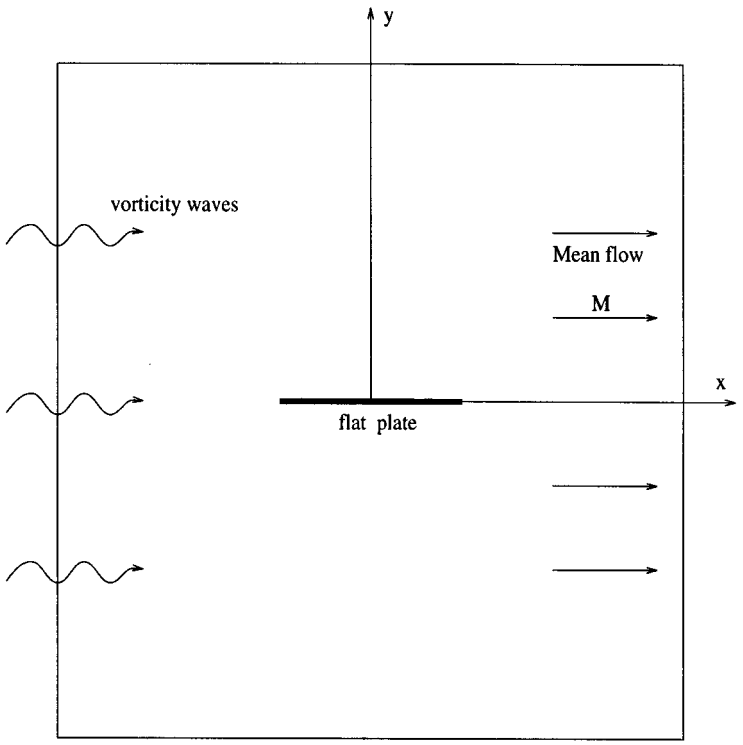

Figure 7. Schematic diagram showing the interaction of a flat plate in a vertical gust.

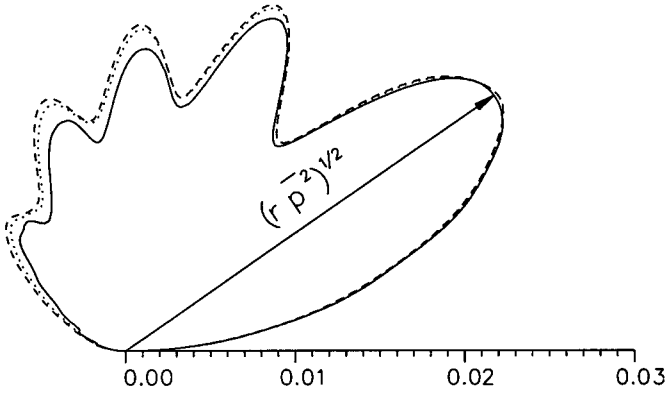

Figure 8. Directivity of sound generated by the interaction of a flat plate in a vertical gust. $\lambda =$ wavelength of incoming gust. —— $\Delta x = \lambda/8$, ... $\Delta x = \lambda/16$, - - - - - $x = \lambda/24$.

conditions have been applied successfully to two benchmark aeroacoustics problems. In this work, only two-dimensional problems have been considered. The methodology, however, can be extended to three-dimensional problems.

ACKNOWLEDGMENTS

This work was supported by NASA Langley Research Center Grant NAG 1-1776.

REFERENCES

1. C.K.W. Tam and J.C. Webb, 'Dispersion-Relation-Preserving finite difference schemes for computational acoustics', *J. Comput. Phys.*, **107**, 262–281 (1993).
2. L.N. Trefethen, 'Group velocity in finite difference schemes', *SIAM Rev.*, **24**, 113–135 (1982).
3. C.K.W. Tam, J.C. Webb and Z. Dong, 'A study of the short wave components in computational acoustics', *J. Comput. Acoustics*, **1**, 1–30 (1993).
4. C.K.W. Tam, 'Computational aeroacoustics: issues and methods', *AIAA J.*, **33**, 1788–1796 (1995).
5. A. Bayliss and E. Turkel, 'Radiation boundary conditions for wave-like equations', *Commun. Pure Appl. Math.*, **33**, 707–725 (1980).
6. A. Bayliss and E. Turkel, 'Far field boundary conditions for compressible flows', *J. Comput. Phys.*, **48**, 182–199 (1982).
7. T. Hagstrom and S.I. Hariharan, 'Accurate boundary conditions for exterior problems in gasdynamics', *Math. Comput.*, **51**, 581–597 (1988).
8. S.I. Hariharan, Y. Ping and J.C. Scott, 'Time domain numerical calculations of unsteady vortical flows about a flat plate airfoil', *J. Comput. Phys.*, **101**, 419–430 (1992).
9. C.K.W. Tam and Z. Dong, 'Radiation and outflow boundary conditions for direct computation of acoustic and flow disturbances in a nonuniform mean flow', *J. Comput. Acoustics*, **4**, 175–201 (1996).
10. K.W. Thompson, 'Time dependent boundary conditions for hyperbolic systems', *J. Comput. Phys.*, **68**, 1–24 (1987).
11. K.W. Thompson, 'Time dependent boundary conditions for hyperbolic systems, II', *J. Comput. Phys.*, **89**, 439–461 (1990).
12. T.J. Poinsot and S.K. Lele, 'Boundary conditions for direct simulations of compressible viscous flows', *J. Comput. Phys.*, **101**, 104–129 (1992).
13. B. Engquist and A. Majda, 'Radiation boundary conditions for acoustic and elastic wave calculations', *Commun. Pure Appl. Math.*, **32**, 313–357 (1979).
14. B. Engquist and A. Majda, 'Absorbing boundary conditions for difference approximations to the multi-dimensional wave equation', *Math. Comput.*, **47**, 629–651 (1986).
15. R.L. Higdon, 'Absorbing boundary conditions for difference approximations to the multi-dimensional wave equation', *Math. Comput.*, **47**, 629–651 (1986).

16. R.L. Higdon, 'Numerical absorbing boundary conditions for the wave equations', *Math. Comput.*, **49**, 65–90 (1987).
17. H. Jiang and Y.S. Wong, 'Absorbing boundary conditions for second order hyperbolic equations', *J. Comput. Phys.*, **88**, 205–231 (1990).
18. R. Kosloff and D. Kosloff, 'Absorbing boundary conditions for wave propagation problems', *J. Comput. Phys.*, **63**, 363–376 (1986).
19. T. Colonius, S.K. Lele and P. Moin, 'Boundary conditions for direct computation of aerodynamic sound generation', *AIAA J.*, **31**, 1574–1582 (1993).
20. D. Givoli, 'Non-reflecting boundary conditions', *J. Comput. Phys.*, **94**, 1–29 (1991).
21. R. Hixon, S.H. Shih and R.R. Mankbadi, 'Evaluation of boundary conditions for computational aeroacoustics', *AIAA J.*, **33**, 2006–2012 (1995).
22. M.B. Giles, 'Non-reflecting boundary conditions for Euler equation calculations', *AIAA J.*, **28**, 2050–2058 (1990).
23. K.A. Kurbatskii and C.K.W. Tam, 'Cartesian boundary treatment of curved walls for high-order computational aeroacoustics finite difference schemes', *AIAA J.*, **35**, 133–140 (1997).

